

Transmission of 120 Gbaud QAM with an All-Silicon Segmented Modulator

Zibo Zheng, Abdolkhalegh Mohammadi, Omid Jafari, Hassan Sepehrian, Xiaoguang Zhang, Wei Shi, and Leslie A. Rusch

IEEE Journal of Lightwave Technology, (published on 08 June 2022)

© 2022 IEEE. Personal use of this material is permitted. Permission from IEEE must be obtained for all other uses, in any current or future media, including reprinting/republishing this material for advertising or promotional purposes, creating new collective works, for resale or redistribution to servers or lists, or reuse of any copyrighted component of this work in other works.

Transmission of 120 Gbaud QAM with an All-Silicon Segmented Modulator

Zibo Zheng, Abdolkhalegh Mohammadi, Omid Jafari, Hassan Sepehrian, Xiaoguang Zhang, Wei Shi, *Senior Member, IEEE, Optica*, and Leslie A. Rusch, *Fellow, IEEE, Fellow, Optica*

Abstract—Segmenting a silicon modulator can substantially increase its electro-optic bandwidth without sacrificing modulation efficiency. We demonstrate a segmented silicon IQ modulator and experimentally explore both modulator design and operating point to optimize systems trade-offs in coherent detection. An electro-optic bandwidth of greater than 40 GHz is measured for a 4-mm-long segment, and greater than 60 GHz for a 2-mm-long segment. We evaluate optical transmission experimentally at 120 Gbaud for 16-ary quadrature amplitude modulation (QAM) and 32QAM. The segments are operated in tandem with identical data at each segment. We present an experimental method to align data timing between the segments. Through the optimization of segment biasing and linear compensation, we have achieved a bit error rate (BER) of 16QAM well below the 20% forward error correction (FEC) threshold (2×10^{-2}). Adding nonlinear pre-compensation allows for 32QAM with a BER below the 24% FEC threshold (4.5×10^{-2}), enabling a net rate of 483 Gbs per polarization. The modulator can also be operated as an optical digital analogy converter for complex optical signal generation, for which 100 Gbs is achieved for a proof of concept.

Index Terms—high baud rate transmission, silicon modulator, segmented modulator, system optimization

I. INTRODUCTION

OPTICAL transmission system must keep up with the rapidly increasing demand of global data traffic. The Ethernet interface has reached 400 Gbs and is moving towards the terabits level. Commercial systems using coherent detection can achieve net bit rates to 800 Gbps with 95 Gbaud symbol rates [1]. Data transmission beyond 1 Tbs has been demonstrated [2]–[5] in the laboratory and field trials. Increasing of capacity in single-carrier transmission has mainly been achieved using high baud rate.

The silicon photonics (SiP) platform has been drawn considerable interest due to its low power consumption, footprint and compatibility with complementary metal-oxide-semiconductor (CMOS) foundries. It has become a prime candidate for next generation optical communications transceivers [6], [7]. High-baud-rate silicon Mach-Zehnder modulators (MZMs) have been demonstrated for both intensity modulation/direct detection (IM/DD) [8]–[11] and coherent detection systems [12], [13]. However, due to silicon limitations, silicon Mach-Zehnder modulator (MZM) have limited V_π , leading to higher

loss than other popular materials such as indium phosphide (InP) and lithium niobate (LiNO₃) [14]. We must trade-off bandwidth performance and V_π to optimize design parameters targeting high speed optical transmission [15]. Segmenting the modulator can sidestep this trade-off.

Segmentation structures have been proposed over several decades, including the concept of “optical digital-to-analog converter (DAC)”, which generates multi-level signal optically and avoid using expensive electrical DAC [16]. On the SiP platform, segmenting a modulator can improve modulation efficiency by increasing the total length of phase shifter in MZM. The MZM benefits for a higher bandwidth provided by the constituent short segments. In [17], three different architectures of silicon MZM were evaluated. The authors tested the performance of pulse-amplitude modulation (PAM) signaling and concluded that the segmented modulator offered clear advantages over the single segment. Following an initial segmented silicon modulator with IM/DD in [18] [19], a 200 Gbs/ λ net rate data transmission was reported [20]. Two segments were utilized for an 80 Gbaud PAM8 modulation.

The MZM phase shifter length determines both efficiency and bandwidth. Better efficiency requires a longer phase shifter but yields lower bandwidth. Segmenting leads to higher bandwidth without losing efficiency. The efficiency is maintained by having the segments combine their effects to produce the same total phase shift as without segmenting. We apply segmenting to push bit rates via wider bandwidth and enhanced signal-to noise ratio from more efficient modulation.

There have been a few reports on coherent detection with segmented modulators in the literature [21] [22]. For single segment SiP MZM, we demonstrated [23] 100 Gbaud 32QAM transmission with coherent detection. With a segmented architecture, we now push the symbol rate beyond 100 Gbaud to further increase capacity. To the best of our knowledge, we report the first examination of a segmented all-silicon device for baud rate beyond 100 GB. High symbol rate transmission has become a important part of next-generation optical communication system. Experimental demonstration over 100 Gbaud symbol rate has been reported [24] [25]. More recently, 200 Gbaud symbol rate PS-64QAM has been achieved with thin-film LiNO₃ modulator leads to 1.6 Tbs capacity [26].

In this paper, we will extent our previous work from [27]. We characterize electro-optical (E-O) response of two segments and quantify the 3 dB bandwidth for various biases. We present system optimization including RF signal alignment, bias optimization and channel compensation. We transmit

Z. Zheng, A. Mohammadi, O. Jafari, H. Sepehrian, L. A. Rusch, and W. Shi are with Department of Electrical and Computer Engineering, COPL, Université Laval, Québec, Canada. (Corresponding author: rusch@gel.ulaval.ca)

X. Zhang is with State Key Laboratory of Information Photonics and Optical Communications, Beijing University of Posts and Telecommunications, Beijing, China

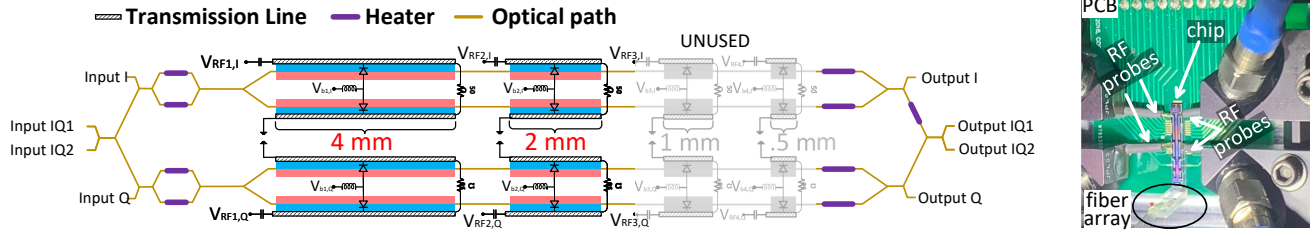


Fig. 1. Left: schematic diagram of segmented modulator design. Right: photograph of fabricated chip, fiber array, RF probes and printed circuit board.

16QAM and 32QAM with 120 Gbaud symbol rate, with coherent detection and single polarization. We adopt the gain-based iterative learning control (G-ILC) [28] [29] nonlinear pre-compensation to mitigate pattern dependent distortion [30] of 32QAM. The BER of 32QAM falls below the 25% FEC threshold, which leads to 483 Gbs net data rate. To the best of our knowledge, this is the first demonstration of 120 Gbaud 32QAM using an all-silicon modulator.

II. MODULATOR DESIGN AND CHARACTERIZATION

The schematic of our segmented modulator design is shown in Fig. 1. Each MZM has four phase shifters (also called segments), each with a distinct length. The segment lengths are 4 mm, 2 mm, 1 mm and 0.5 mm. Two identical MZM interferometers of four segments (I branch on top, and Q branch below) are combined 90° out of phase to form an IQ modulator. In our transmission experiment two longest segments are used, the 4 mm and 2 mm segments.

Laterally doped p-n junctions in 220 nm-high silicon rib waveguides are used as the phase shifters. Three levels of dopants are applied to reduce the junction resistance without introducing excess optical loss. The MZM uses traveling-wave (TW) electrodes in a series push-pull driving configuration, which enables lower capacitive load for a higher bandwidth. Each TW-phase shifter uses a coplanar stripline transmission line with on-chip 50 Ω termination implemented using semiconductor resistors. The SiP modulator was fabricated using a CMOS-compatible process on a 220 nm silicon-on-insulator wafer with 2 μm buried oxide. Further design details can be found in [15].

The chip has multiple optical input/output (IO) for flexible tuning and characterization. There are independent optical inputs for the in-phase and quadrature (I/Q) branches, as well as a common IQ input. We can thermally tune on-chip heaters located near the optical inputs to maximum the MZM extinction ratio and to tune the operating point. Optical loss on the MZM is around 21.5 dB, including ~12 dB fiber-to-chip coupling and ~3 dB from the long waveguide routing.

Our choice to only examine two segments (4 mm and 2 mm) is motivated by limitations in RF resources and system complexity. In the rest of paper, we will refer to the 4 mm segment as the “long segment” and the 2 mm segment as the “short segment”. We measure the E-O frequency response (S21) of the long and short segments on each branch (I and Q) at various bias voltages, using a 67 GHz vector network analyzer (VNA) (model Agilent N5227) and a on-chip calibration substrate. We route the VNA signal to the chip through a

RF cable and probe, each with a 3 dB bandwidth of 67 GHz. The MZM optical output is converted to the electrical domain with a 70 GHz balanced photodetector (BPD) (Finisar) and routed to the VNA. The cables and probe were characterized separately and their frequency response was de-embedded from the characterization of individual modulators.

Figure 2(a) shows results for the Q-branch long segment, Fig. 2(b) for the short segment, and Fig. 2(c) reports the system response. The system response includes all filtering effects from devices and digital signal processing (DSP) equalization. While measurements reported in Fig. 2(a,b) were collected with the VNA, the system response was estimated from captured data, as explained further in the next paragraphs.

The E-O responses of I and Q branches showed similar results, so we present only the Q branch results to save space. We examined four bias voltages, with an S21 curve for each voltage in Fig. 2(a) and (b). After de-embedding, we find the 3 dB bandwidth of the long segment is 41 GHz at 3V reverse bias, and 43 GHz at 5 V reverse bias. As expected, the shorter segment has greater 3 dB bandwidth: 58 GHz at 2 V and 62.75 GHz at 5V bias.

During transmission experiments reported in section IV we identified the bias voltages for each arm that minimized the BER (3 V for the long segment, 2 V for the short segment). While higher voltages yielded higher 3 dB bandwidth, they did not improve BER. In Fig. 2(a) and (b) we focus attention on the relevant curves (bias that optimized BER) by putting a shaded box around the bias voltage annotations.

We next characterized the system response when using the two segments in tandem. The two segments had identical driving signals, but distinct bias voltages. Note that the system response is the combined response of the MZM, cables, probes and photodetector; de-embedding was not possible. The solid black line in Fig. 2(c) reports the frequency response at the optimum bias voltages. Individual segment responses with the complete system are also reported, with square markers for the long segment and diamond markers for the short segment. The tandem frequency response when using both segments falls between long and short ones, essentially trading off bandwidth for better BER. This trade-off favors the short segment frequency response, i.e., it falls closer to that curve. Hence, we do not lose much bandwidth performance by using both two segments in tandem rather than the short segment alone.

In addition to the tandem system response, we also show individual SiP MZM responses with dash lines. For easy reference, we include segment responses de-embedded from other

system components, i.e., repeated from Fig. 2(a) and Fig. 2(b), with asterisk markers and triangle markers, respectively. We can see in this figure that our system response is limited not by the SiP chip, but rather by the RF loss from components such as the RF cables and probe. Hence, our transmission results should be interpreted in this light.

III. EXPERIMENTAL SETUP

The experimental setup for modulation is shown in Fig. 3(a). We generate a random QAM signal offline and shape it by a raised cosine filter with roll-off factor 0.01. We use four high speed DAC modules to generate these electrical signals at 120 Gbaud. The Micram DAC has a maximum 128 GSa/s sampling rate and 8-bit resolution [25]. We operate the DAC at 120 GSa/s, i.e., one sample per symbol. We adopt digital pre-compensation for the DAC response and residual ripple in the optical channel after optical filtering. The pre-compensation is a finite impulse response (FIR) filter estimated from a series of characterizations of the electrical back-to-back performance and optical transmission performance [31].

Each pair of two DAC outputs is identical, but the pairs have independent data: one pair for the I branch of the long and short segments, and another pair for the Q branch. Each output has an RF power amplifier (model SHF 804B) to deliver around 3 Vpp to the RF probe driving the segmented IQ modulator. Each DAC output has a phase shifter for fine alignment of RF signal timing at each segment; the long and short segments should have identical signals that are well synchronized despite any variations in the length of electrical cabling.

On the optical side, an external cavity laser (ECL) operating at 1548 nm with 100 kHz linewidth is boosted to 28 dBm optical signal-to-noise ratio (OSNR) by a high power erbium doped fiber amplifier (EDFA). We couple the light to the silicon chip via a fiber array and on-chip grating coupler, which introduces 12 dB loss. The modulator introduces an additional 10 dB of insertion loss. We use a two-stage EDFA to boost the chip output before reception.

We place an optical filter (Finisar Waveshaper) between the two-stage optical amplifier. The programmable optical filter not only suppresses out-of-band amplified spontaneous noise (ASE), but also to equalize the silicon modulator frequency response [23] [31]. We place a variable optical attenuator (VOA) after the two-stage EDFA to control received optical power at the coherent receiver. Higher optical power mitigates thermal noise from the receiver and achieves better error rate performance. We sweep the power and present results in Section V. Two BPD with 70 GHz bandwidth are connected after coherent receiver. A Keysight real-time oscilloscope (RTO) with 160 GSa/s sampling rate and 63 GHz bandwidth captures electrical data from BPD.

Captured data is processed via offline DSP. A low-pass filter eliminates out-of-band noise. We resample the captured data to four samples per symbol for further processing. We use data-aided timing synchronization. We apply the constant modulus algorithm (CMA) for coarse estimation, followed by multi-modulus algorithm (MMA); the filters have $T_s/4$ spaced taps

in a 2x2 multiple-input multiple-output (MIMO) configuration. The MIMO algorithm compensates residual inter-symbol interference (ISI) and recovers polarization; this mitigates most of the linear impairments in the signal. We sweep the number of MIMO taps and find 35 taps are sufficient for CMA and MMA. We downsample the signal after MIMO to one sample per symbol for frequency offset compensation (FOC). We use a blind phase search Carrier phase recovery (CPR). We apply separate linear decision-directed minimum mean square error (MMSE) equalizers to the I and Q coordinates.

We also employ nonlinear techniques at the receiver to improve BER. We apply a Volterra polynomial nonlinear equalizer and a maximum likelihood sequence detection (MLSD) with one-tap post filter. the Volterra polynomial includes 1st and 3rd order terms; and the polynomial coefficients are estimated with a DD-MMSE with 255 taps. Our one-tap post filter has transfer function $H(z) = 1 + \beta z^{-1}$; β is swept and we find 0.5 to be optimal for both 16QAM and 32QAM.

At the transmitter, we employ nonlinear pre-distortion by using G-ILC technique to mitigate pattern-dependent distortion. The green path in Fig. 3 shows the quasi-real-time adaptation of G-ILC with hardware-in-the-loop. The principle of the G-ILC is to take a fixed block of data and to pre-distort this data block. The pre-distorted block is found experimentally during multiple iterations (typically a dozen iterations over 30-40 minutes of data capture). The error between reference and recovered symbols is used during adaptation. All nonlinear techniques are described in detail in our previous publication [23]. We estimate the channel response from captured data from receiver DSP. The system bandwidth performance in Fig.2(c) are estimated by data-aided MMSE algorithm from captured data. See [15] for the details.

The setup is configured as complex signal (i.e., QAM) transmission with a single polarization state. We sometimes turn on only of the branches (I or Q), but capture the data by the same coherent receiver, i.e., we sometimes use amplitude shift keying (ASK) signaling with coherent detection. For example, we use one branch to optimize reverse DC bias for each segment, or for some performance analysis. In all cases, we operate the IQ modulator at the null point.

IV. SYSTEM OPTIMIZATION AND SIMULATION

A. RF signal synchronization

In our tandem drive experiment, two separate but identical RF signals drive each segment in a branch. Proper modulation requires that the segments have phase shifts that swing in concert, i.e., with zero timing offset. Differences in the physical paths of the two signals can be corrected by working with both/either an tunable RF delay and/or a delay function in the DAC. The digital delay in the DAC is used to correct to within one symbol interval (coarse). The tunable RF delay line is used to tune within a symbol interval (fine).

A pseudo-random bit sequence is used for synchronization. We send two drive signals (two DAC outputs) to one branch (I or Q). We sweep the symbol delay in the pseudo random binary sequence (PRBS) between the two DAC channels, which sweeps the residual delay at the segments. As we sweep,

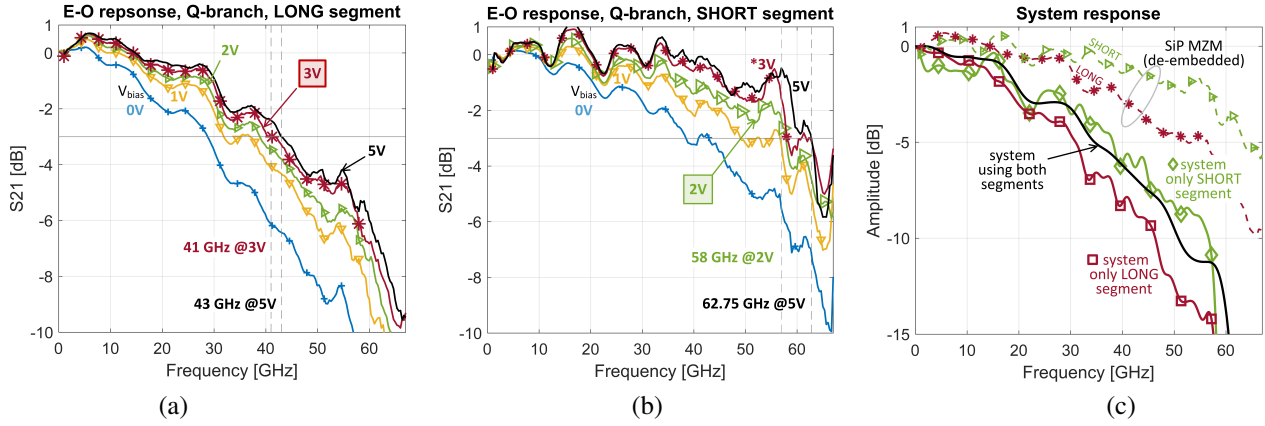


Fig. 2. Frequency response of a) long MZM segment with de-embedding for various bias voltages, b) short MZM segment with de-embedding for various bias voltages, c) system responses at optimal bias voltages.

we observe the optical spectrum. For large residual delay the signals are uncorrelated and the spectrum is flat. When the residual delay is within one symbol delay the spectrum is most peaked, with deep notches. We fix the PRBS delay between the two DAC outputs at this value.

For fine synchronization, we observe the spectrum under two scenarios sketched in Fig. 4(a). The symbol τ represents the time delay introduced by the manually tuned RF phase shifter. In the DAC, we delay the PRBS in the two DAC outputs by one symbol interval: in scenario one the long segment leads, in scenario two the short segment leads. When the delay is properly tuned, the two scenarios will yield identical spectra, as in the upper spectra in Fig. 4(a). If we have the worst case delay, the output will appear as the lower spectra. We alternate between the two scenarios while tuning the phase shifter. When both scenarios give identical spectra, we fix the RF phase shifter. The two-symbol-period delay is sufficient to perturb the spectra in an easily identifiable manner, but another delay could also be used.

B. Bias optimization

The DC bias impacts the bandwidth and the modulation efficiency. We sweep the bias voltage on the modulator while observing BER to find the best trade-off between bandwidth and efficiency [23]. For a segmented modulator, the bias should be optimized for each segment. Our design has two segments in each (in-phase/quadrature) branch, or four segments in total. For simplicity, we only perform pairwise optimization (long and short segments jointly) in each branch, rather than searching independently across four biases.

Using the setup in Fig. 3, we turn off the upper branch by driving it with a sequence of zeros. The lower branch has a PRBS synchronized across the long and short segments as we sweep the two bias settings from 0 to 4V. We measure OSNR (before VOA) with an optical spectrum analyzer (OSA) with a 0.1 nm bandwidth resolution. We recover the data and use the MMSE filter to estimate the noise equivalent bandwidth.

We report in Fig. 5 results for 25 combinations of biases. We present the OSNR in dB in Fig. 5(a), the noise equivalent

bandwidth [32] in GHz in Fig. 5(b), and the symbol error rate (SER) in Fig. 5(c). The OSNR is best for low bias, while the bandwidth is best at high bias. While the OSNR exhibits a symmetry vis-à-vis the long and short segment bias, this is not the case for bandwidth. The long segment bias has a much greater impact: when the long segment has low bias the short segment bias has little effect on the overall bandwidth. In the tandem configuration, the overall bandwidth falls between the extremes of the long and short segment bandwidths (see Fig. 2(c)). Interestingly, the frequency response (after optimizing the biases of the two segments for best SER performance) is closer to the wideband, short segment. This we attribute to the significantly improved modulation efficiency by using two segments, allowing us to push to greater bandwidth in optimizing the bandwidth-efficiency trade-off.

Since the OSNR is optimized in the bottom-left corner, and the bandwidth in the top-right corner, we examine SER in Fig. 5(c) to find the best trade-off for these two parameters. The SER matrix does not exhibit any clear symmetry. The lowest SER appears at (3V,2V), in a mid-section of swept biases. At this operating point the SER is around 2×10^{-3} ; the reduced OSNR is offset by greater bandwidth and thus less attenuation of the ASK4 data signal at 120 Gbaud. Figure 5(d) presents a typical recovered ASK4 signal. Results were similar when optimizing the upper branch.

C. Linear pre-equalization

We fix the operating point to the optimal biases we identified. We next optimize the channel compensation in both the electrical and the optical domain using linear techniques. Digital FIR filters will be applied in the electrical domain at the transmitter. We use a programmable optical band-pass filter (Waveshaper) for optical compensation. Using techniques inspired by [31] but adapted to a segmented modulator, we optimize performance by balancing the filter depths as described in the following.

We see in Fig. 2(c) that individually the long (square markers) and short (diamond markers) segments have different E-O responses at the optimal bias. The tandem operation of

both segments yields yet another overall E-O response (black line, no markers). Pre-compensation seeks to equalize the response. If we simply base our compensation filter on the overall response, each segment will not see a flat response. This may cause ISI. Therefore we adopt another strategy.

We compensate each segment individually in the electrical domain, and jointly in the optical domain. We smooth the short segment filter in the frequency domain: the total response is a sum of the smoothed filter and a residual ripple. The smooth version is used in the optical filter. The residual ripple will be implemented electrically on the short segment drive signal.

The long segment filter is partitioned into the smoothed short segment filter and a residue. Again, the residue will be compensated electrically. The decomposed frequency responses are illustrated in Fig. 6(a). The ripple goes to the short segment electrical FIR and fluctuates around 0 dB. The two remaining filters have depths referenced to 0 dB: α is the depth of the long segment residue electrical FIR, and γ is the depth of optical filter with the smooth response. The long segment has a pre-compensation filter with greater depth due to its faster roll-off at high frequency. The depth $\alpha \sim 5$ dB corresponds to the additional attenuation at 60 GHz for the long segment compared to the short segment.

Having determined the digital FIR filters, the two segments will be roughly equalized and have a similar response that can be compensated by a single common optical filter. We must find the appropriate depth γ for the joint optical filter. We sweep γ while transmitting 16QAM at 120 Gbaud. The BER is estimated for each γ and plotted in Fig. 6(a); 6.5 dB gives best QAM BER. Received electrical spectrum with and without channel compensation are shown in Fig. 6(b). Channel compensation brings normalized signal power up by about 10 dB at the highest frequency. The received spectrum before and after linear pre-compensation is shown in Fig. 6(c); the compensation yields a fairly flat spectrum.

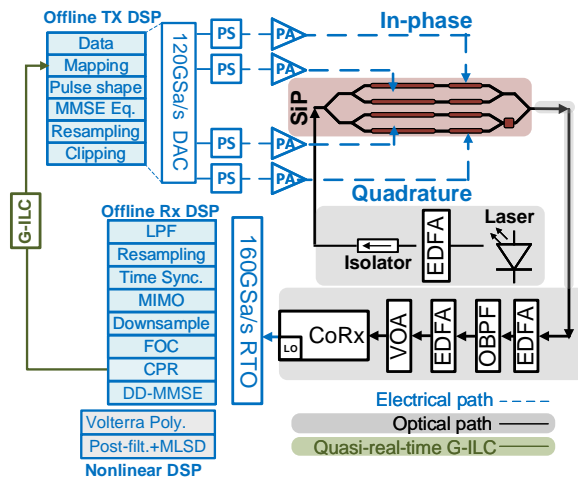


Fig. 3. Block diagram of optical transmission setup including DSP stack on TX/RX. PS: phase shifter; PA: power amplifier; OBPF: optical band-pass filter; EDFA: erbium-doped fiber amplifier; VOA: variable optical attenuator

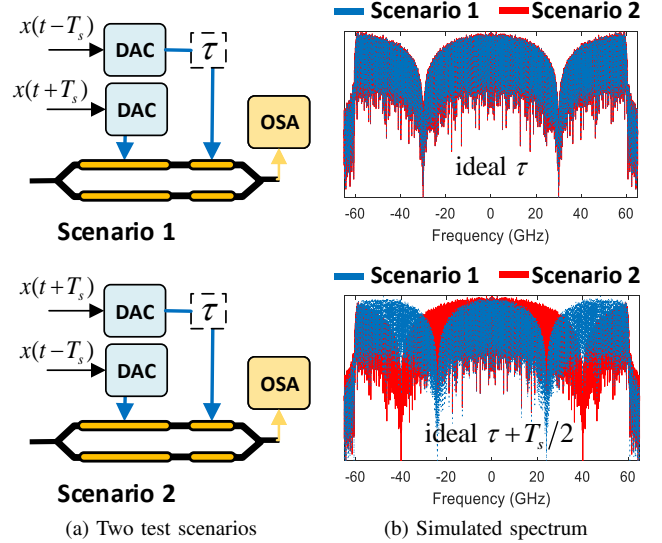


Fig. 4. Simulation of spectral effects in the presence of timing delay, (a) block diagram and two sets of drive signals (scenario 1: input $x(t-T_s)$ and $x(t+T_s)$ signals to short and long segment; scenario 2: swap input signals of scenario 1); and (b) spectra of scenario 1 (red) and scenario 2 (blue) for ideal delay (above) and worst case delay (below).

V. QAM TRANSMISSION RESULTS

We transmit 16QAM and 32QAM at 120 Gbaud. Random QAM symbols are sent to the DAC: two copies of the real part destined for the I branch, and two copies of the imaginary part destined for the Q branch. As described in Section IV.C, the signals for the short segments have one digital pre-compensation filter applied, while the signals for the long segments have another applied. We use the optimal bias found in Section IV.B for each segment: 3 V for the long segments and 2 V for the short segments. The RF skew between signals in a given branch are carefully synchronized as described in Section IV.A. Note that identical data is sent to the long and short segments of a branch, but the signals differ as different filtering are applied.

We measured the OSNR of the modulated QAM signal with an OSA at 0.1 nm resolution. The maximum OSNR was around 28 dB. We estimated BER for 16QAM and 32QAM from a measurement of more than 400,000 symbols. Recovery of modulation order above 32 was not possible due to the limited OSNR. At the receiver we apply the DSP chain listed in Fig. 3 and described in Section III. The post-compensation techniques are deployed consecutively; we examine performance after each post-compensation step to assess the impact on BER performance.

Consider first the 16QAM results in Fig. 7. We plot BER versus received optical power when using various post-compensation techniques in DSP. The poorest performance (black curve, asterisk markers) is recorded when only using the MIMO MMA after carrier recovery. When we add equalization via a linear MMSE filter (blue curve, circle markers) we see improvement. The BER does not much improve when we add the Volterra polynomial (orange curve, diamond markers). Adding a final stage of one-tap MLSD (purple curve, square

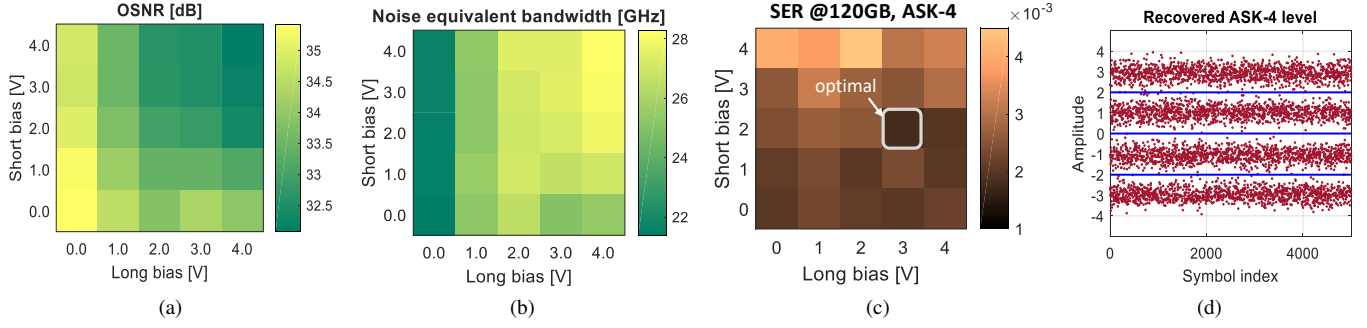


Fig. 5. ASK4 at 120 Gbaud on lower branch of MZM with swept bias on the long and short segments yields (a) OSNR, (b) noise equivalent bandwidth, which are estimated received data (c) SNR and (d) recovered symbols (points) and hard-decision thresholds (lines) at optimum bias of (3V,2V).

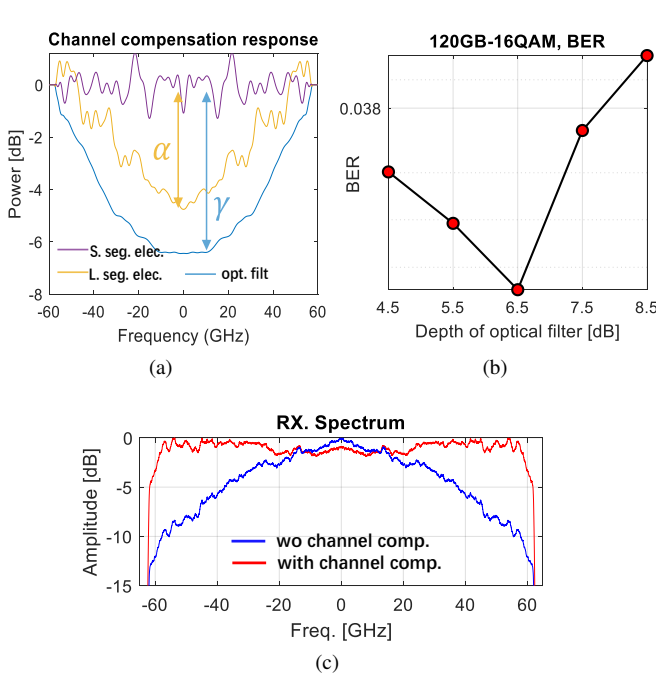


Fig. 6. Linear channel equalization techniques. (a) Decomposition on channel inverse response for segmented modulator. Purple and yellow lines: different pre-compensation filter are applied to electrical channel for long/short segment; blue line: public optical filter response. (b) BER versus optical filter depth, operating at 120Gbaud-16QAM. (c) Electrical spectrum from receiver, with (red line) and without (blue line) channel compensation.

markers) leads to the best performance. We note that for received optical power as low as -6 dBm, all solutions have performance below the 20% FEC threshold of 2.4×10^{-2} BER.

Consider next 32QAM. No nonlinear pre-compensation at the transmitter, i.e., G-ILC, was needed for 16QAM. In contrast, without the G-ILC method the BER of 32QAM remained around 6×10^{-2} and could not be further optimized by post-compensation. The G-ILC pre-compensation was found experimentally in quasi-real-time in 11 training iterations [30]. We present in Fig. 8(a) the convergence curve for training, i.e., mean squared error versus iterations.

Per the 32QAM BER curves in Fig. 7, with G-ILC nonlinear pre-compensation we achieved 32QAM performance below the 24% FEC threshold at $\text{BER} \sim 4.5 \times 10^{-2}$ [33]. The soft-decoding performance of this time-invariant spatially coupled

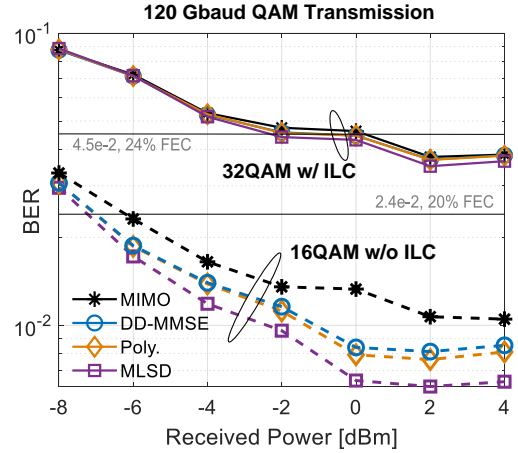


Fig. 7. BER vs. received optical power for 16QAM without ILC (dashed curves) and 32QAM with ILC (solid curves). Four post-compensation are examined: the MMA alone; when adding DD-MMSE; when adding a Volterra polynomial to the two previous steps; and when adding a final stage of MLSD.

low-density parity-check (LDPC) code was demonstrated experimentally on 64QAM transmission. We can see that the post-compensation had little effect on performance; the use of nonlinear pre-compensation was key. The best BER achieved was 3.6×10^{-2} at 4 dBm received power.

We present recovered constellations at 4 dBm received power, and focus on the impact of pre-compensation. In all cases we use the strictly linear post-processing, i.e., no Volterra and no MLSD. The 16QAM constellation with no G-ILC is shown in Fig. 8(b). Constellations of 32QAM without and with G-ILC pre-compensation are presented in Fig. 8(c) and (d), respectively. The blocky clusters in the 32QAM constellation in Fig. 8(c) is due to hard decision of DD-MMSE. When using G-ILC, the constellation clusters becomes more circular and the BER improves. Unlike 16QAM, nonlinear post-compensation provided very little improvement for 32QAM due to both insufficient SNR and stronger pattern dependent distortion. This behavior is consistent with that observed in [23].

In Fig. 9 we compare the effective SNR versus received power for the best-case DSP for each of our transmission rates. The effective SNR was estimated from the recovered constellations with knowledge of the true transmitted symbols.

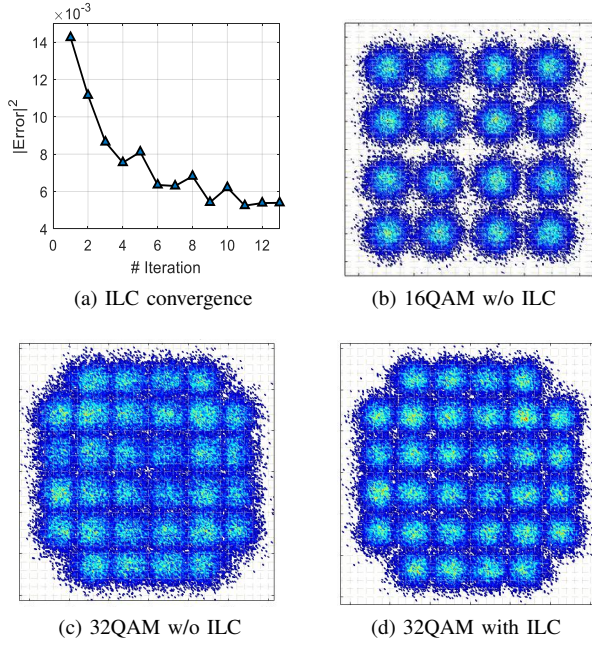


Fig. 8. Curve on MSE versus ILC iteration. Constellation of recovered 16QAM (without ILC) and 32QAM (without and with ILC) are also shown

The mode at each symbol was used to find symbol power, and the effective SNR is found from averaging over SNR per symbol. We note that the SNR was estimated before MLSD processing.

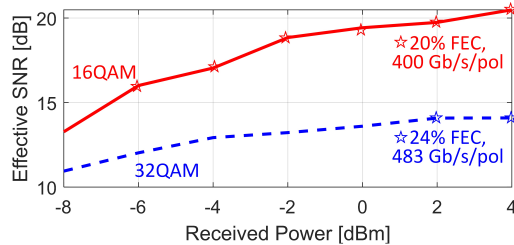


Fig. 9. Effective SNR vs. received optical power for best-case DSP

VI. DISCUSSION

A. Optical DAC drive scheme

In the demonstrations reported here, we used identical PAM4 signals sent to two segments of different length. We used an electrical DAC to generate PAM4 and to apply electronic pre-equalization *and* multilevel modulation. Multilevel modulation can be achieved without an electrical DAC; independent binary (not four level) signals are sent to each segment [16], [20], [34]. Avoiding an electrical DAC reduces system complexity

The drive voltage and bias settings of each segment can be manipulated to create the proper amplitude on each segment so that the combined output is equally spaced four level signals. This concept is illustrated in Fig. 10. A larger RF power on the long segment leads to large space between output binary levels. At the next, shorter segment a smaller RF power leads to a second modulation, or four output power levels. In a

SiP modulator, we tune the DC bias on the p-n junction and the RF swing to optimize output signal. Finding the optimal parameters minimizing bit error is very time-consuming to.

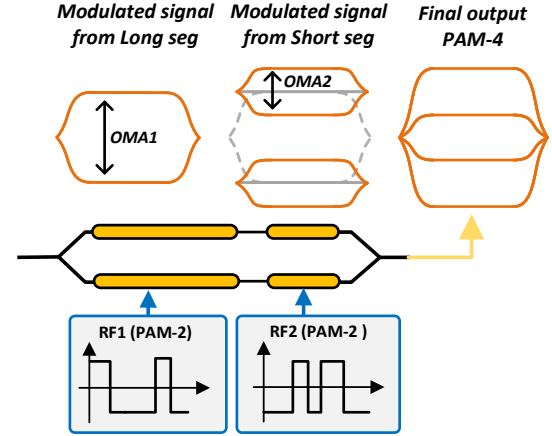


Fig. 10. Optical DAC using two PAM2 signals to generate PAM4; RF1 and RF2 (below the block diagram) are binary, independent electrical signals with different PAM2 pattern. Amplitude levels (boxes above the block diagram) respect $OMA1 = 2 \times OMA2$, OMA: optical modulation amplitude.

For operation at 100 Gbaud and higher, the electrical DAC is unavoidable; it is not needed for forming multiple levels, but rather to shape the pulse at 100 Gbaud to fall in the passband of the modulator and thereby avoid intersymbol interference. Combining the two DAC approaches (i.e., independent data per segment) could enhance the signal during the electro-optical conversion. We applied this method to both the in-phase and quadrature branches to create a 16QAM output from four independent binary drive signals.

We observed slightly worse performance than those previously presented. Sample constellations for 16QAM at 100 Gbaud are given in Fig. 11. In Fig. 11(a) we achieve multilevel signaling with the optical DAC and we achieve pre-compensation with the electrical DAC. In Fig. 11(b) we achieve both with an electrical DAC. The BER was roughly doubled when using the optical DAC configuration. The same setup and DSP were applied for both configurations. We did not include optical channel compensation nor electrical compensation of the modulator. We did not attempt to modify the electrical compensation to further optimize BER as the adjustment of RF power and bias was already complex.

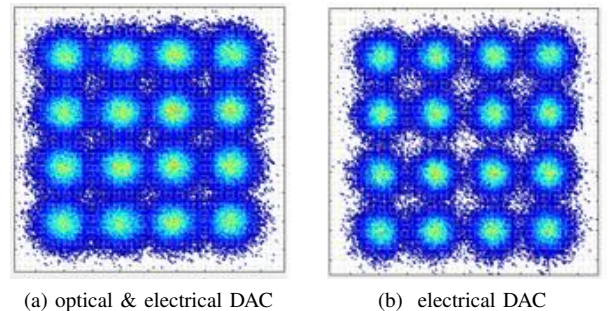


Fig. 11. 100 Gbaud 16QAM transmission results by (a) electrical and optical DAC scheme and (b) electrical DAC scheme.

Ideally, we should trade-off constellation distortion and final SNR by an optimal choice of RF swing and DC bias. This is experimentally very challenging, and we only minimize the constellation distortion, as in [20]. We cannot draw firm conclusions about which approach is best. The optical DAC has low complexity and low quantization noise, while the electrical DAC has more straightforward signal compensation.

B. Synchronization between segments

Segmented modulators are inherently demanding for drive signal synchronization, as even a small offset leads to visible degradation in the quality of the modulated signal. This is particularly important in crafting an integrated solution [35]. We do a simple back-to-back simulation of an additive white Gaussian noise (AWGN) channel to examine the impact of imperfect synchronization on BER performance. We apply identical PAM4 signals to two MZM segments. The MZM is modelled as a simple sinusoidal function of the input RF signal, i.e., $E_{out} \propto \exp(V/V_\pi)$. The SNR is set to 15 dB and no any bandwidth limitation is simulated. The BER degradation is presented in Fig. 12. For delay larger than $0.5 T_s$, the BER sees nearly exponential increase.

For a noise free-signal, i.e., very large SNR, we present MZM output eye diagrams in Fig. 12 for perfect synchronization as compared to a half symbol delay. We clearly see the degradation in the single sampling point of zero delay, to the thickened version with $0.5 T_s$ delay. As the this simulation is noise-free, this is caused solely by distortion induced by poor synchronization. This delay is relative to the symbol interval; the absolute synchronization requirement becomes more demanding as symbol rate increases. Taking 120 Gbaud as an example, $0.5 T_s$ is 4 ps.

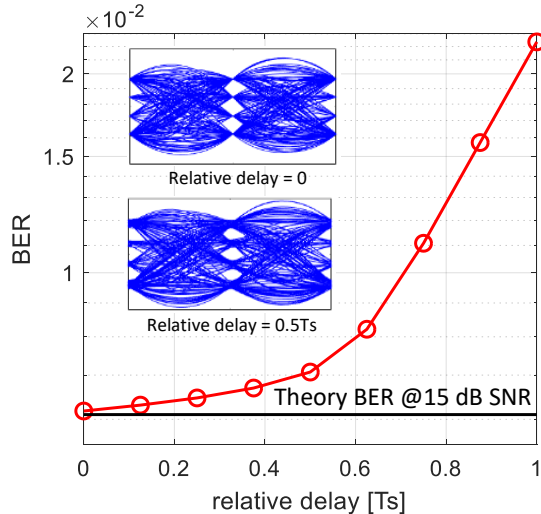


Fig. 12. PAM4, 15 dB SNR, AWGN channel simulation of BER versus drive signal timing delay; insets are noise-free eye diagrams for two delays; T_s : symbol period time.

Our experimental demonstration achieved alignment by manually manipulating the input signal and observing the optical spectrum on OSA. This could be achieved using digital signal processing instead, avoiding the use of an OSA. Data

captured under the two scenarios could be compared to create an error signal. For instance, we also used this technique in the laboratory and achieved similar timing precision with 16 sample-per-symbol (SPS) capture. Similarly, the RF delay can be manipulated digitally. Time skew between drive signals can be pre-compensated at the transmitter by adding phase shift in frequency domain. However, phase shift in frequency domain will tend to increase peak-to-average power ratio (PAPR) in time domain waveform, which may affect signal power output from the DAC. A trade-off between system complexity and performance can be found in the digital domain, and is not a serious obstacle to exploitation of segmented modulators.

VII. CONCLUSION

We presented the design of a segmented IQ modulator and experimental results for 120 Gbaud 32QAM optical back-to-back transmission with two segments. We characterized the E-O responses of a 4 mm (long) and a 2 mm (short) segment on a fabricated chip. We measured a 3-dB bandwidth on the 4 mm segment greater than 40 GHz; the 2 mm reached above 60 GHz. We introduced an RF signal synchronization process. We optimized the bias and channel compensation to achieve the lowest BER. We demonstrated 120 Gbaud optical back-to-back transmission of 16QAM and 32QAM signal on a single polarization. We achieved 16QAM with BER of 6.4×10^{-3} with linear pre-compensation and nonlinear post-compensation. For 32QAM we reached BER of 3.6×10^{-2} by additional nonlinear pre-compensation G-ILC; this is lower than 24% FEC threshold. The 120 Gbaud 32QAM results indicate a net rate per polarization of 483 Gbs. Finally, we discussed the option to use an optical DAC drive scheme, and implementation issues.

APPENDIX

We characterize the V_π of the long and short segments with 0V reverse bias on the pn-junction. We first apply 0V also to the RF probe. We sweep the C-band and measured the power at each wavelength, creating the baseline spectrum. We next applied a fixed DC voltage on the RF electrode, and again measured the spectrum. A typical trace is shown in Fig. 13a for the 4 mm segment. From this plot we find the phase shift in radians, with a π phase shift scaled as indicated.

We characterize each segment and record the phase shifts when sweeping the DC voltage applied to the RF electrode from zero to 10V. We plot the phase shift versus applied voltage in Fig. 13b. Measured values are given in markers, while the dashed lines give a linear fit. We can see that the curve for the 4 mm segment hits π phase shift at 9.2V. The 2 mm segment reaches 0.5π shift at around 8V. By extrapolation, the V_π would be 16V. These estimates of V_π lead to 3.6 V-cm and 3.2 V-cm modulation efficiency for 4 mm and 2 mm segments, respectively.

ACKNOWLEDGMENT

The authors would like to acknowledge operating funds NSERC Canada (CRDPJ528381) and a fabrication subsidy

from CMC Microsystems. We also thank our technician Simon Levasseur for packaging and technical support.

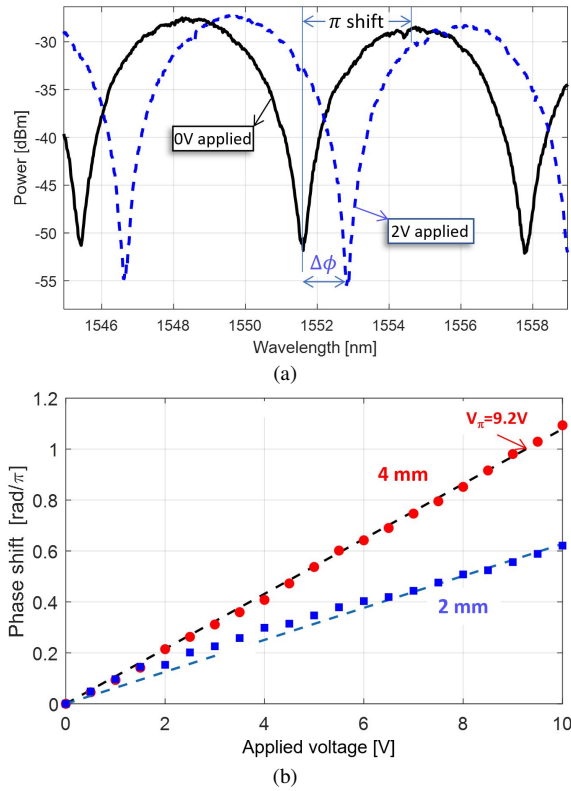


Fig. 13. a) Typical spectra during characterization of the 4 mm segment, and b) phase shift vs. applied voltage for each segment.

REFERENCES

- [1] Infinera Breaks Industry Record with 800G Transmission over 950 Kilometers in a Live Network Trial. [Online]. Available: <https://www.infinera.com/press-release/infinera-breaks-industry-record-with-800g-transmission-over-950-kilometers-in-a-live-network-trial/>
- [2] F. Buchali, K. Schuh, R. Dischler, M. Chagnon, V. Aref, H. Buelow, Q. Hu, F. Pulka, M. Frascolla, E. Alhammedi, A. Samhan, I. Younis, M. El-Zonkoli, and P. Winzer, "1.3-Tb/s single-channel and 50.8-Tb/s WDM transmission over field-deployed fiber," in *Proc. Euro. Conf. Opt. Commun.*, 2019, pp. 1–4.
- [3] A. Matsushita, M. Nakamura, S. Yamamoto, F. Hamaoka, and Y. Kisaka, "41-Tbps C-band WDM transmission with 10-bps/Hz spectral efficiency using 1-Tbps/ λ signals," *J. Lightw. Technol.*, vol. 38, no. 11, pp. 2905–2911, 2020.
- [4] G. Raybon, A. Adamiecki, J. Cho, P. Winzer, A. Konczykowska, F. Jorge, J.-Y. Dupuy, M. Riet, B. Duval, K. Kim, S. Randel, D. Piliro, B. Guan, N. Fontaine, and E. C. Burrows, "Single-carrier all-ETDM 1.08-Terabit/s line rate PDM-64-QAM transmitter using a high-speed 3-bit multiplexing DAC," in *IEEE Photon. Conf. (IPC)*, 2015, pp. 1–2.
- [5] F. Buchali, K. Schuh, R. Dischler, M. Chagnon, V. Aref, H. Buelow, Q. Hu, F. Pulka, M. Frascolla, I. Younis, M. El-Zonkoli, and P. Winzer, "DCI Field Trial Demonstrating 1.3-Tb/s Single-Channel and 50.8-Tb/s WDM Transmission Capacity," *J. Lightw. Technol.*, vol. 38, no. 9, pp. 2710–2718, 2020.
- [6] W. Shi, Y. Tian, and A. Gervais, "Scaling capacity of fiber-optic transmission systems via silicon photonics," *Nanophotonics*, vol. 9, no. 16, pp. 4629–4663, 2020.
- [7] C. Doerr and L. Chen, "Silicon photonics in optical coherent systems," *Proceedings of the IEEE*, vol. 106, no. 12, pp. 2291–2301, 2018.
- [8] M. S. Alam, X. Li, M. Jacques, Z. Xing, A. Samani, E. El-Fiky, P.-C. Koh, and D. V. Plant, "Net 220 Gbps/IM/DD Transmission in O-band and C-band with silicon photonic Traveling-Wave MZM," *J. Lightw. Technol.*, vol. 39, no. 13, pp. 4270–4278, 2021.
- [9] W. Shi, Y. Xu, H. Sepehrian, S. LaRochelle, and L. A. Rusch, "Silicon photonic modulators for PAM transmissions," *J. Opt.*, vol. 20, no. 8, p. 083002, 2018.
- [10] H. Zhang, M. Li, Y. Zhang, D. Zhang, and et al., "800 Gbit/s transmission over 1 km single-mode fiber using a four-channel silicon photonic transmitter," *Photon. Res.*, vol. 8, no. 11, pp. 1776–1782, Nov 2020.
- [11] F. Zhang, L. Zhang, X. Ruan, F. Yang, H. Ming, and Y. Li, "High Baud Rate Transmission With Silicon Photonic Modulators," *IEEE J. Sel. Topics Quantum Electron.*, vol. 27, no. 3, pp. 1–9, 2021.
- [12] S. Zhalehpour, J. Lin, M. Guo, H. Sepehrian, Z. Zhang, L. Rusch, and W. Shi, "All-silicon IQ modulator for 100 Gbaud 32QAM cases," in *Proc. Opt. Fiber Commun. Conf. (OFC)*, 2019.
- [13] J. Zhou, J. Wang, L. Zhu, and Q. Zhang, "Silicon Photonics for 100Gbaud," *J. Lightw. Technol.*, vol. 39, no. 4, pp. 857–867, 2021.
- [14] M. Jacques, A. Samani, D. Patel, E. El-Fiky, M. Morsy-Osman, T. Hoang, M. G. Saber, L. Xu, J. Sonkoly, M. Ayliffe, and D. V. Plant, "Modulator material impact on chirp, DSP, and performance in coherent digital links: comparison of the lithium niobate, indium phosphide, and silicon platforms," *Opt. Express*, vol. 26, no. 17, pp. 22471–22490, 2018.
- [15] H. Sepehrian, J. Lin, L. A. Rusch, and W. Shi, "Silicon Photonic IQ Modulators for 400 Gb/s and Beyond," *J. Lightw. Technol.*, vol. 37, no. 13, pp. 3078–3086, 2019.
- [16] M. Papuchon, C. Puech, and A. Schnapper, "4-bits Digitally Driven Integrated Amplitude Modulator for Data Processing," *Electron. Lett.*, vol. 16, no. 4, pp. 142–144, 1980.
- [17] A. Samani, E. El-Fiky, M. Morsy-Osman, R. Li, D. Patel, T. Hoang, M. Jacques, M. Chagnon, N. Abadia, and D. V. Plant, "Silicon photonic Mach-Zehnder Modulator Architectures for on Chip PAM-4 Signal Generation," *J. Lightw. Technol.*, vol. 37, no. 13, pp. 2989–2999, 2019.
- [18] A. D. Simard, B. Filion, D. Patel, D. Plant, and S. LaRochelle, "Segmented silicon MZM for PAM-8 transmissions at 114 Gb/s with binary signaling," *Opt. Express*, vol. 24, no. 17, pp. 19467–72, 2016.
- [19] A. Samani, D. Patel, M. Chagnon, E. El-Fiky, R. Li, M. Jacques, N. Abadia, V. Veerasubramanian, and D. V. Plant, "Experimental parametric study of 128 Gb/s PAM-4 transmission system using a multi-electrode silicon photonic Mach Zehnder modulator," *Opt. Express*, vol. 25, no. 12, pp. 13252–13262, 2017.
- [20] M. Jacques, Z. Xing, A. Samani, E. El-Fiky, X. Li, M. Xiang, S. Lessard, and D. V. Plant, "240 Gbit/s Silicon Photonic Mach-Zehnder Modulator Enabled by Two 2.3-Vpp Drivers," *J. Lightw. Technol.*, pp. 2877–2885, 2020.
- [21] A. Shastri, C. Muzio, M. Webster, G. Jeans, P. Metz, S. Sunder, B. Chattin, B. Dama, and K. Shastri, "Ultra-Low-Power Single-Polarization QAM-16 Generation Without DAC Using a CMOS Photonics Based Segmented Modulator," *J. Lightw. Technol.*, vol. 33, no. 6, pp. 1255–1260, 2015.
- [22] G. R. Mehrpoor, C. Schmidt-Langhorst, B. Wohlfeil, R. Elschner, D. Rafique, R. Emmerich, A. Dochhan, I. Lopez, P. Rito, D. Petousi et al., "64-GBd DP-Bipolar-8ASK transmission over 120 km SSF employing a monolithically integrated driver and MZM in 0.25- μ m SiGe BiCMOS technology," in *Proc. Opt. Fiber Commun. Conf. (OFC)*, 2019, pp. Tu2A–5.
- [23] S. Zhalehpour, M. Guo, J. Lin, Z. Zhang, Y. Qiao, W. Shi, and L. A. Rusch, "System Optimization of an All-Silicon IQ Modulator: Achieving 100 Gbaud Dual Polarization 32QAM," *J. Lightw. Technol.*, vol. 38, no. 2, pp. 256–264, 2019.
- [24] M. Nakamura, F. Hamaoka, M. Nagatani, H. Yamazaki, T. Kobayashi, A. Matsushita, S. Okamoto, H. Wakita, H. Nosaka, and Y. Miyamoto, "104 Tbps/carrier probabilistically shaped PDM-64QAM WDM transmission over 240 km based on electrical spectrum synthesis," in *Proc. Opt. Fiber Commun. Conf. (OFC)*, 2019, pp. M41–4.
- [25] F. Buchali, V. Aref, R. Dischler, M. Chagnon, K. Schuh, H. Hettrich, A. Bielik, L. Altenhain, M. Guntermann, R. Schmid, and M. Moller, "128 GSa/s SiGe DAC Implementation Enabling 1.52 Tb/s Single Carrier Transmission," *J. Lightw. Technol.*, vol. 39, no. 3, pp. 763–770, 2021.
- [26] X. Chen, G. Raybon, D. Che, J. Cho, and K. Kim, "Transmission of 200-Gbaud PDM Probabilistically Shaped 64-QAM Signals Modulated via a 100-GHz Thin-film LiNbO₃ I/Q Modulator," in *Proc. Opt. Fiber Commun. Conf. Exhib. (OFC)*, 2021, paper F3C–5.
- [27] Z. Zheng, A. Mohammadi, O. Jafari, H. Sepehrian, J. Lin, X. Zhang, L. A. Rusch, and W. Shi, "Silicon IQ Modulator for 120 Gbaud QAM," in *Proc. Euro. Conf. Opt. Commun.*, 2021, pp. 1–4.
- [28] J. Chani-Cahuana, P. N. Landin, C. Fager, and T. Eriksson, "Iterative Learning Control for RF Power Amplifier Linearization," *IEEE Trans. Microw. Theory Techn.*, vol. 64, no. 9, pp. 2778–2789, 2016.

- [29] M. Schoukens, J. Hammenecker, and A. Cooman, "Obtaining the Preinverse of a Power Amplifier Using Iterative Learning Control," *IEEE Trans. Microw. Theory Techn.*, vol. 65, no. 11, pp. 4266–4273, 2017.
- [30] S. Zhalehpour, J. Lin, H. Sepehrian, W. Shi, and L. A. Rusch, "Mitigating pattern dependent nonlinearity in SiP IQ-modulators via iterative learning control predistortion," *Opt. Express*, vol. 26, no. 21, pp. 27 639–27 649, 2018.
- [31] J. Lin, H. Sepehrian, L. A. Rusch, and W. Shi, "Single-carrier 72 GBaud 32QAM and 84 GBaud 16QAM transmission using a SiP IQ modulator with joint digital-optical pre-compensation," *Opt. Express*, vol. 27, no. 4, pp. 5610–5619, 2019.
- [32] M. Usher, "Noise and bandwidth," *J. Phys. E: Sci. Instrum.*, vol. 7, no. 12, p. 957, 1974.
- [33] F. Buchali, A. Klekamp, L. Schmalen, and T. Drenski, "Implementation of 64QAM at 42.66 GBaud using 1.5 samples per symbol DAC and demonstration of up to 300 km fiber transmission," in *Proc. Opt. Fiber Commun. Conf. (OFC)*, 2014, pp. M2A–1.
- [34] O. Jafari, S. Zhalehpour, W. Shi, and S. LaRochelle, "DAC-Less PAM-4 Slow-Light Silicon Photonic Modulator Assisted by Coupled Bragg Grating Resonators," in *Proc. Opt. Fiber Commun. Conf. (OFC)*, 2021, paper Th1D–6.
- [35] F. Zhang, Y. Zhu, F. Yang, L. Zhang, X. Ruan, Y. Li, and Z. Chen, "Up to single lane 200G optical interconnects with silicon photonic modulator," in *Proc. Opt. Fiber Commun. Conf. (OFC)*, 2019, paper Th4A–6.

Zibo Zheng (Student member, IEEE) received the M.Sc. degree in telecommunication and management from Beijing University of Posts and Telecommunication (BUPT) in 2016. He studies for Ph.D degree in BUPT since 2016 and continue working on it in Université Laval, Québec, QC, Canada from Fall, 2019. His research interests include optical transmission system, digital signal processing, signal compensation and recovery, Silicon photonics modulator and transmission application.

Abdolkhalegh Mohammadi Abdolkhalegh Mohamadi was born in Shiraz, Iran, in 1987. He received his B.S. degree in Electrical Engineering from Shiraz University, Iran, in 2009. He got his M.Sc. degree in Telecommunication Engineering from Urmia University, Iran, in 2012. Currently he is doing his Phd degrees in Centre d'optique, photonique et laser (COPL), Université Laval working on Electro-Optic Modulators. His research interests include Silicon photonic transceivers, Optical communication, and Microwave photonics.

Omid Jafari received the M.Sc. degree in electrical engineering (microwave photonic) from the Sharif University of Technology, Tehran, Iran, in 2014. He received his Ph.D degree in electrical and computer engineering from the Université Laval, Québec, QC, Canada, in 2021. His research interests include nano-/micro-photonics devices, CMOS-photonics codesign, and high-speed optical communications.

Hassan Sepehrian (S'08) received the Ph.D. degree in electrical and computer engineering from the Université Laval, Québec, QC, Canada, in 2018. He is currently with Huawei Technologies Canada. His research interests include silicon photonics, integrated electronic-photonics systems for high-capacity optical transmissions, and analog/mixed-signal integrated circuits.

Xiaoguang Zhang (Senior Member, IEEE) was born in Beijing, China, in June 1961. He received the B.S. and M.S. degrees in physics from Peking University, Beijing, in 1985 and 1988, respectively, and the Ph.D. degree in physical electronics from the Beijing University of Posts and Telecommunication, Beijing, in 2004. From 1988 to 2008, he was a Professor in physics with the Department of Physics, School of Science, Beijing University of Posts and Telecommunications, where he is currently a Professor with the Institute of Information Photonics and Optical Communications. He is the author or coauthor of more than 200 international journals (including IEEE and OSA journals) and peer-reviewed conference papers (including OFC, ECOC, CLEO, and APOC), and holds more than 20 China patents. His research interests include polarization effects in fibers, multilevel phase modulation formats, recovery of optical signal distortions, and generation of optical frequency comb.

Leslie Ann Rusch (S'91–M'94–SM'00–F'10) received the B.S.E.E. degree (Hons.) from the California Institute of Technology, Pasadena, CA, USA, in 1980 and the M.A. and Ph.D. degrees in electrical engineering from Princeton University, Princeton, NJ, USA, in 1992 and 1994, respectively. She currently holds a Canada Research Chair in Communications Systems Enabling the Cloud with the Department of Electrical and Computer Engineering, Université Laval (UL), Québec, QC, Canada. She is a member of the Centre for Optics, Photonics and Lasers at UL. From 1980 to 1990, she was a Communications Project Engineer with the Department of Defense. While on leave from Université Laval, she spent two years (2001–2002) with Intel Corporation creating and managing a group researching new wireless technologies. She has published more than 150 articles in international journals (90% IEEE/OSA) with wide readership, and contributed to more than 195 conferences. Her articles have been cited over 6500 times per Google Scholar. Her research interests include digital signal processing for coherent detection in optical communications using silicon photonic devices, spatial multiplexing using orbital angular momentum modes in fiber, radio over fiber and OFDM for passive optical networks; and in wireless communications, supporting 5G over passive optical networks and optimization of the optical/wireless interface in emerging cloud based computing networks. Dr. Rusch is the recipient of the IEEE Canada Fessenden award for Contributions to Telecommunications. She was also the recipient of numerous awards for graduate training, including the IEEE Canada Ham Award for Graduate Supervision. She was the Vice President of Technical Affairs on the Board of Governors of IEEE Photonics Society. She has served on multiple technical program committees for major international conferences, and as an Associate Editor for the IEEE/OSA Journal of Optical Communications Networks and the IEEE Communications Letters. She is Fellow of Optica.

Wei Shi (S'07–M'12) received the Ph.D. degree in electrical and computer engineering in 2012 from the University of British Columbia, Vancouver, BC, Canada, where he was awarded the BCIC Innovation Scholarship for a collaboration entrepreneurship initiative. He is currently an Associate Professor with the Department of Electrical and Computer Engineering and a member of Centre for Optics, Photonics and Lasers (COPL), Université Laval, Québec, QC, Canada. Before joining Université Laval in 2013, he was a Researcher with McGill University, Montreal, QC, Canada, where he held a Postdoctoral Fellowship with the Natural Sciences and Engineering Research Council of Canada (NSERC). He holds a Canada Research Chair in Silicon Photonics. His current research interests include integrated photonic devices and systems, involving silicon photonics, nanophotonics, CMOS-photonics co-design, high-speed optical communications, chip-scale lasers, and optical sensors.